Observation of *A*-site antiferromagnetic and *B*-site ferrimagnetic orderings in the quadruple perovskite oxide $CaCu_3Co_2Re_2O_{12}$

Zhehong Liu,[1,2] Xiao Wang,[1,3] Xubin Ye,[1,2] Xudong Shen,[1,2] Yuecheng Bian,[4] Wei Ding,[4] Stefano Agrestini,[3,5] Sheng-Chieh Liao,[3] Hong-Ji Lin,[6] Chien-Te Chen,[6] Shih-Chang Weng,[6] Kai Chen,[7] Philippe Ohresser,[7] Lucie Nataf,[7] Francois Baudelet,[7] Zhigao Sheng,[4] Sonia Francoual,[8] José R. L. Mardegan,[8] Olaf Leupold,[8] Zefang Li,[1,2] Xuekui Xi,[1,2] Wenhong Wang,[1,2] Liu Hao Tjeng,[3] Zhiwei Hu,[3] and Youwen Long[1,2,9,*]

[1]*Beijing National Laboratory for Condensed Matter Physics, Institute of Physics, Chinese Academy of Sciences, Beijing 100190, China*

[2]*School of Physical Sciences, University of Chinese Academy of Sciences, Beijing 100049, China*

[3]*Max Planck Institute for Chemical Physics of Solids, Nöthnitzer Straße 40, 01187 Dresden, Germany*

[4]*Anhui Key Laboratory of Condensed Matter Physics at Extreme Conditions, High Magnetic Field Laboratory, Chinese Academy of Sciences, Hefei 230031, China*

[5]*Diamond Light Source, Harwell Science and Innovation Campus, Didcot, OX11 0DE, United Kingdom*

[6]*National Synchrotron Radiation Research Center, Hsinchu 30076, Taiwan*

[7]*Synchrotron SOLEIL, L'Orme des Merisiers, Saint-Aubin, 91192 Gif-sur-Yvette Cedex, France*

[8]*Deutsches Elektronen-Synchrotron DESY, Notkestraße 85, 22607 Hamburg, Germany*

[9]*Songshan Lake Materials Laboratory, Dongguan, Guangdong 523808, China*

(Received 13 May 2020; revised 22 November 2020; accepted 22 December 2020; published 12 January 2021)

A quadruple perovskite oxide $CaCu_3Co_2Re_2O_{12}$ was synthesized by high-pressure annealing. This compound crystallizes in an *A*- and *B*-site ordered quadruple perovskite structure with space group *Pn*-3. The charge combination is determined to be $CaCu^{2+}{}_3Co^{2+}{}_2Re^{6+}{}_2O_{12}$ by bond valence sum analysis and x-ray absorption spectroscopy. In contrast to other isostructural $ACu_3B_2B'_2O_{12}$ compounds with a single magnetic transition, a long-range antiferromagnetic phase transition originating from the *A*′-site Cu^{2+} sublattice is found to occur at $T_N \approx 28$ K. Subsequently, the spin coupling between the *B*-site Co^{2+} and *B*′-site Re^{6+} ions contributes to a ferrimagnetic transition around $T_C \approx 20$ K. Strong electrical insulating behavior is identified by optical measurement with an energy gap of approximately 3.75 eV. The mechanisms of the spin interactions are discussed in detail.

DOI: 10.1103/PhysRevB.103.014414

I. INTRODUCTION

A-site ordered quadruple perovskites, which have the chemical formula $AA'_3B_4O_{12}$, exhibit a wide variety of intriguing physical properties, such as high-temperature ferromagnetic (FM) or ferrimagnetic (FiM) ordering [1–4], charge disproportionation [5,6] colossal magnetoresistance [7], intermetallic charge transfer [5,6], half metallicity [1,3,4], negative thermal expansion [5,6], huge dielectric constant [8,9], multiferroicity, etc. [10,11]. In contrast to a simple ABO_3 perovskite, where the *A* site is usually occupied by a large-size nonmagnetic alkali-metal, alkaline-earth, or lanthanide cation, the *A*′ site in an *A*-site ordered quadruple perovskite can be occupied by a magnetic transition metal (TM) ion with a smaller ionic radius. As a result, heavily tilted BO_6 octahedra and square-coordinated $A'O_4$ units form. The TM ions with a strong Jahn-Teller distortion, such as Cu^{2+} and Mn^{3+}, occupy the *A*′ site favorably. The different electronic configurations between $Mn^{3+}(t_{2g}{}^3e_g{}^1)$ and $Cu^{2+}(t_{2g}{}^6e_g{}^3)$ ions often produce different magnetic and electrical transport properties in $AMn^{3+}{}_3B_4O_{12}$ and $ACu^{2+}{}_3B_4O_{12}$. In general, two independent long-range antiferromagnetic (AFM) orderings, arising from the *A*′-site Mn^{3+} ions or *B*-site TM ions, take place in $AMn_3B_4O_{12}$ [11–13], whereas a single FM-like phase transition occurs in $ACu^{2+}{}_3B_4O_{12}$ [7,14,15]. Exceptionally, in $CaCu_3Ti_4O_{12}$, $CdCu_3Ti_4O_{12}$, and $CaCu_3Zr_4O_{12}$ with nonmagnetic d^0 TM ions at the *B* sites, the *A*′-site Cu^{2+} spins induce an AFM transition at lower temperatures [9,16].

Furthermore, if another TM ion *B*′ is used to partially substitute the *B* site in an $ACu^{2+}{}_3B_4O_{12}$ compound, one may obtain both *A*- and *B*-site ordered quadruple perovskite $ACu^{2+}{}_3B_2B'_2O_{12}$. To date, long-range spin ordering in the reported *A*- and *B*-site ordered perovskites have always been observed to display a $Cu^{2+}(\uparrow)B(\uparrow)B'(\downarrow)$-type FiM coupling [1–3,17–19]. Moreover, compared with the relative $A_2BB'O_6$ double perovskite, the quadruple one usually has a much higher spin ordering temperature. For example, the FiM phase transition temperature T_C sharply increases from approximately 320 K in Ca_2FeOsO_6 to 580 K in $CaCu_3Fe_2Os_2O_{12}$, raising the possibility of potential applications for these magnetic functional materials well above room temperature (RT) [1,2,20]. At present, there is no reported long-range AFM ordering of the *A*′-site Cu^{2+} in the $ACu^{2+}{}_3B_2B'_2O_{12}$ family. In this study, we prepared an alternative *A*-site and *B*-site ordered quadruple perovskite $CaCu_3Co_2Re_2O_{12}$ (CCCRO) with the

*Corresponding author: ywlong@iphy.ac.cn

charge combination of $CaCu^{2+}{}_3Co^{2+}{}_2Re^{6+}{}_2O_{12}$. Unexpectedly, the A'-site Cu^{2+} experiences an AFM phase transition at 28 K, and then a FiM ordering occurs around 20 K as a result of the $Co^{2+}(\uparrow)Re^{6+}(\downarrow)$ coupling.

II. EXPERIMENTAL DETAILS

Polycrystalline $CaCu_3Co_2Re_2O_{12}$ was synthesized by a high-pressure and high-temperature method. High-purity (>99.9%) powders of CaO, CuO, Co_3O_4, ReO_2, and Re_2O_7 with mole ratio 9:27:6:10:4 were taken as starting materials and mixed thoroughly in an agate mortar. The powder mixture was pressed into a gold capsule of 3-mm diameter and 4.0-mm length, and then treated at 7 GPa and 1323 K for 30 min on a cubic anvil-type high-pressure apparatus. x-ray powder diffraction (XRD) was measured using a Huber diffractometer with Cu$K\alpha_1$ radiation at 40 kV and 30 mA. The XRD data were refined by the Rietveld method using the GSAS software [21]. The Cu-$L_{2,3}$ and Co-$L_{2,3}$ x-ray absorption spectroscopy (XAS) were measured at RT using the total electron yield mode of beamline TLS11A at the NSRRC synchrotron facility in Taiwan. The Re-L_3 XAS spectrum was measured with the transmission mode at RT on beamline TLS07A of the NSRRC. The x-ray magnetic circular dichroic (XMCD) spectra at the Cu-$L_{2,3}$ and Co-$L_{2,3}$ edges were measured at 10 K and 6 T on beamline DEIMOS of the synchrotron SOLEIL in Paris. The Re-$L_{2,3}$ XMCD spectra were measured at 5 K and 5 T on P09 beamline of PETRA III (shown in this work) and 10 K and 1.3 T on beamline ODE of SOLEIL (not shown). The magnetic susceptibility and magnetization data were collected using a superconducting quantum interference magnetometer (Quantum Design, MPMS) operating in vibrating sample magnetometer mode. Both zero-field-cooling (ZFC) and field-cooling (FC) modes were used to measure the magnetic susceptibility in the range 2–300 K at a magnetic field $H = 0.01$ T. Magnetization was measured at fields ranging from -7 to 7 T at selected temperatures 2, 24, 50, and 300 K. The specific heat (C_p) was measured by a pulse relaxation method on a physical property measurement system (Quantum Design, PPMS-9T). Different magnetic fields (0, 3, and 5 T) were applied for C_p measurements from 50 to 2 K. Nuclear magnetic resonance (NMR) was measured at variable temperatures and a magnetic field of 9.39 T with Bruker Avance III 400 HD. The UV-vis diffuse reflection spectrum was measured by an ultraviolet−visible−near-infrared spectrophotometer (UV−vis−NIR, Cary-5E).

III. RESULTS AND DISCUSSION

Figure 1(a) shows the XRD pattern and the refined result for CCCRO. The presence of the sharp diffraction peaks corresponding to crystal indices with an odd-numbered total value $h + k + l$ [such as (111), (311), and (333)] provide convincing evidence for the rocksalt-type ordered distribution of Co/Re cations at the B/B' sites. Rietveld analysis confirmed the high-pressure product CCCRO to be an A-site and B-site ordered quadruple perovskite structure with space group Pn-3 [see Fig. 1(b)]. In this symmetry, the A-site Ca and A'-site Cu atoms occupy the special Wyckoff sites 2 a (0.25, 0.25, 0.25) and 6 d (0.25, 0.75, 0.75) with ratio 1:3, and the B-site Co and B'-site Re atoms are also orderly distributed at the 4 b (0, 0, 0) and 4 c (0.5, 0.5, 0.5) sites, respectively. During the structure refinement, the occupancy factors for all the cations are almost equal to unity, indicating a negligible antisite occupancy effect. The refined structural parameters are listed in Table I. According to the related bond lengths, the bond valence sum (BVS) calculations give the valence states of Cu and Co as +2.07 and +2.11, respectively, suggesting the formation of Cu^{2+} and Co^{2+}. Because of the absence of the BVS parameter for a Re^{6+} state, we did not calculate the valence state for Re in CCCRO. However, the Re-O bond length (1.892 Å) in CCCRO is similar to that observed in the double perovskite $Sr_2Mg^{2+}Re^{6+}O_6$ (1.912 Å on average). A Re^{6+} charge state is thus expected to occur in the current CCCRO [22]. The high-pressure synthesis condition is responsible for the slightly reduced Re-O distance in CCCRO compared with Sr_2MgReO_6. Therefore, the structural analysis suggests a $CaCu^{2+}{}_3Co^{2+}{}_2Re^{6+}{}_2O_{12}$ charge combination. This will be further investigated using XAS, as shown below.

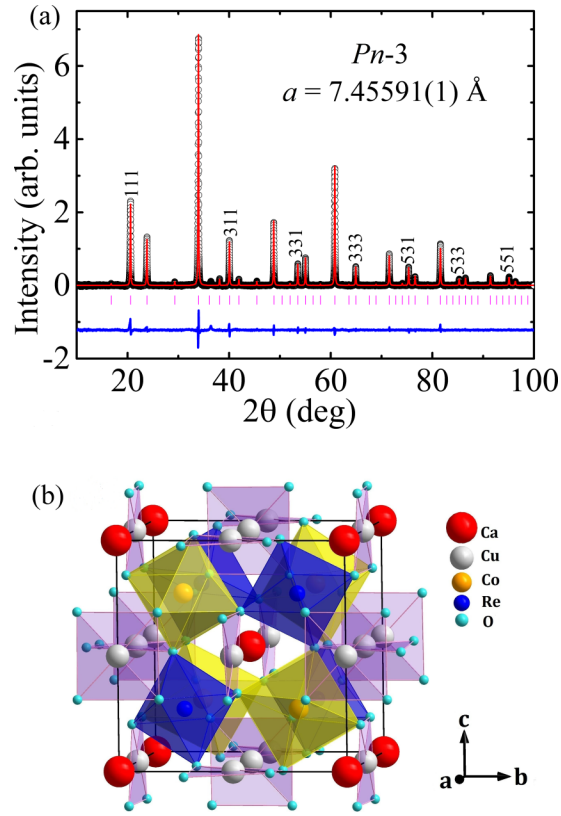

FIG. 1. (a) XRD pattern and structure refinement results for CCCRO at room temperature. The observed (black circles) and calculated (red line) results and their difference (bottom blue line) are plotted. The ticks indicate the allowed Bragg reflections for the Pn-3 space group. (b) Crystal structure of A- and B-site ordered quadruple perovskite CCCRO with Pn-3 symmetry. The corner-sharing Co/ReO_6 octahedra and spatially isolated CuO_4 squares are shown.

Element-selective XAS at the $L_{2,3}$ edges is renownedly highly sensitive to the valence state and the local environment for TMs. Figure 2(a) shows Cu-$L_{2,3}$ XAS for CCCRO together with $CaCu_3Ti_4O_{12}$ as a Cu^{2+} reference in a quadruple perovskite structure [9]. A strong sharp peak is apparent at

TABLE I. Refinement structure parameters for CCCRO and the BVS results for Cu and Co at room temperature. Space group: *Pn*-3; atomic sites: Ca 2*a* (0.25, 0.25, 0.25); Cu 6*d* (0.25, 0.75, 0.75); Co 4*b*(0, 0, 0); Re 4*c* (0.5, 0.5, 0.5); O 24*g* (*x, y, z*). The BVS values (V_i) were calculated as $V_i = \sum_j S_{ij}$, with $S_{ij} = \exp[(r_0 - r_{ij})/0.37]$. We used $r_0 = 1.679$ for Cu and 1.692 for Co. For the *B*-site Co and *B*′-site Re, six coordinated oxygen atoms were used. For the *A*′-site Cu, 12 coordinated oxygen atoms were used in the BVS calculation.

Parameter	CCCRO
a (Å)	7.45595(1)
O_X	0.4454(6)
O_Y	0.9269(5)
O_Z	0.7632(3)
U_{iso}(Ca)(100 × Å^2)	4.8(3)
U_{iso}(Cu)(100 × Å^2)	0.67(5)
U_{iso}(Co)(100 × Å^2)	0.65(3)
U_{iso}(Re)(100 × Å^2)	0.42(1)
U_{iso}(O)(100 × Å^2)	1.1(1)
Cu-O (× 4)	1.968(2)
Co-O (× 6)	2.078(2)
Re-O (× 6)	1.892(2)
∠Co-O-Re (deg)	139.8(1)
∠Cu-O-Re (deg)	113.5(1)
∠Cu-O-Co (deg)	105.9(1)
BVS (Cu)	2.07
BVS (Co)	2.11
R_{wp}	3.1%
R_p	2.0%

930.0 eV for the Cu-L_3 edge, and at 950.0 eV for the L_2 edge for both CCCRO and $CaCu_3Ti_4O_{12}$, indicating that a Cu^{2+} valence state emerges in CCCRO. In other words, the 3*d* shell of the Cu ion has a hole and therefore the Cu ion carries a magnetic moment. We can safely exclude the presence of a nonmagnetic Cu^{1+} valence state as in Cu_2O since the corresponding XAS peak position would be higher by several electronvolts owing to the closed 3*d* shell configuration of Cu^{1+} [23].

To identify the valence state of Co in CCCRO, we exploit the fact that, in open-shell systems, a unitary increase in the valence of the TM ion produces a shift of the $L_{2,3}$ XAS spectrum toward higher energies by approximately 1.0 eV or more [2,24–26]. In the experiment, a CoO single crystal was measured simultaneously for energy reference at the Co-$L_{2,3}$ edges, and a Co^{3+} reference $EuCoO_3$ taken from Ref. [27] was used for comparison. The Co-$L_{2,3}$ XAS spectrum of CCCRO shows up 1.5 eV lower in energy than that of $EuCoO_3$, but has the same energy as for CoO, demonstrating a Co^{2+} valence state in CCCRO. The very similar multiplet spectral features of CCCRO and CoO indicate also the same local coordination of the Co ion. Figure 2(c) shows the Re-L_3 XAS spectrum for CCCRO together with $Sr_2MgRe^{6+}O_6$ and $Sr_2FeRe^{5+}O_6$ as Re^{6+} and Re^{5+} references, respectively [22,28]. Compared with $Sr_2FeRe^{5+}O_6$, the energy position of the Re-L_3 edge of CCCRO is shifted toward higher energies by approximately 1.1 eV, but has the same energy position as for the Re^{6+} reference Sr_2MgReO_6. This demonstrates the Re^{6+} valence state in CCCRO fulfilling the charge-balance requirement. Therefore,

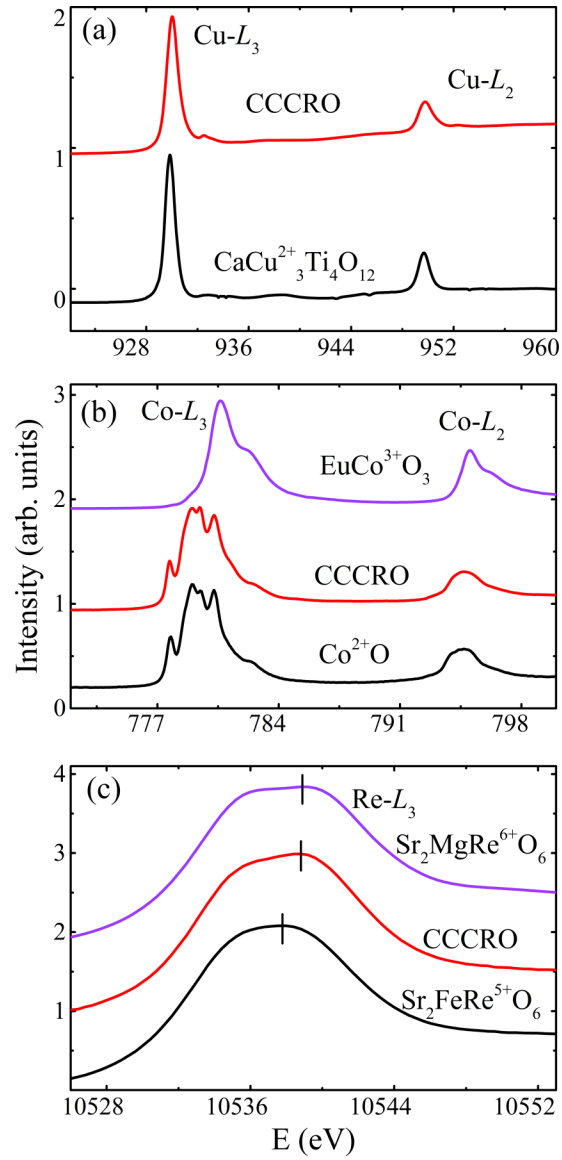

FIG. 2. (a) Cu-$L_{2,3}$ XAS for CCCRO, and $CaCu_3Ti_4O_{12}$ as a Cu^{2+} reference. (b) Co-$L_{2,3}$ spectra for CCCRO, and $EuCoO_3$ as a low-spin Co^{3+} reference (from Ref. [27]) and CoO as a high-spin Co^{2+} reference. (c) Re-L_3 XANES for CCCRO, and Sr_2MgReO_6 as a Re^{6+} reference and Sr_2FeReO_6 as a Re^{5+} reference.

the XAS results confirm the $CaCu^{2+}{}_3Co^{2+}{}_2Re^{6+}{}_2O_{12}$ charge combination, in agreement with the BVS analysis.

Figure 3(a) shows the temperature dependence of the magnetic susceptibility measured at 0.01 T. As the temperature is decreased, the susceptibility displays two anomalies at $T_N \sim 28$ K and $T_C \sim 20$ K, which are more clearly apparent when plotting the derivative of the susceptibility [see the inset of Fig. 3(a)]. Since T_N shifts toward lower temperatures with increasing field during the specific-heat measurement (shown later), an AFM transition is assigned to the anomaly at 28 K. On account of the sharp increase of the magnetic susceptibility below T_C, a FiM or FM phase transition probably occurs at this critical temperature. As shown in Fig. 3(b), the temperature dependence of the inverse susceptibility of CCCRO displays a clear nonlinearity. This

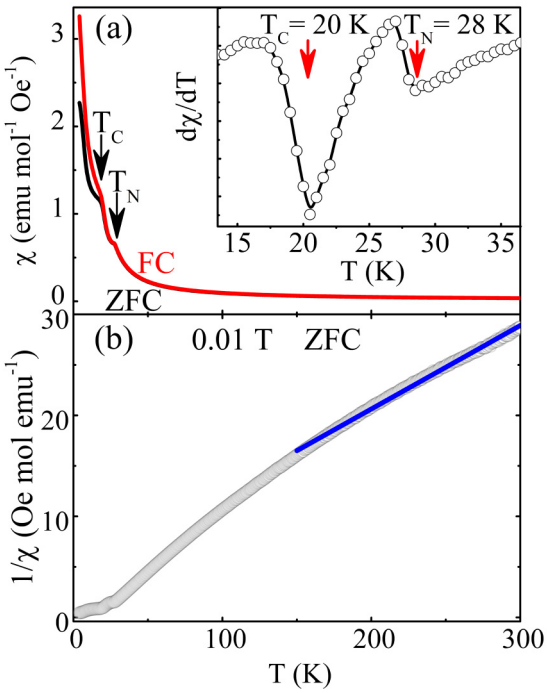

FIG. 3. (a) Temperature dependence of the magnetic susceptibility measured at 0.01 T for CCCRO using ZFC (black) and FC (red) modes. The inset shows the derivative of the susceptibility. (b) Temperature-dependent inverse susceptibility (empty circles) and the Curie-Weiss fitting result from the high-temperature range (blue solid line).

may indicate the presence of an active spin-orbit interaction producing low-lying excited states that can be thermally populated as observed in $LaMn_{0.5}Co_{0.5}O_3$ [29]. Indeed, based on the Curie constant ($C = 12.1$ emu K Oe^{-1} mol^{-1}) fitted in the higher-temperature region, the effective magnetic moment is calculated to be $\mu_{\text{eff}} \approx 9.84\ \mu_B$/f.u. Considering only the spin moment, the theoretical effective moment of CCCRO is 6.71 μ_B/f.u., much less than the fitted value. Once the orbital moments of both Co and Re are included, the effective moment (10.09 μ_B/f.u.) becomes comparable with experiment. Therefore, a considerable orbital moment seems to be generated by the 3*d* Co^{2+} and the 5*d* Re^{6+} ions in CCCRO. We investigated this aspect further using XMCD measurements, as discussed below.

The magnetization behavior provides additional evidence for the double magnetic transitions. As presented in Fig. 4, above T_N, the magnetization depends linearly on the field, as expected for paramagnetic behavior. Below T_C (e.g., 2 K), however, the magnetization increases sharply with the field below about 2 T, before then increasing almost linearly at higher fields. This feature is in accordance with the superimposed AFM and FiM/FM orderings in CCCRO at lower temperatures, as mentioned above. Between T_N and T_C (e.g., 24 K), the magnetization deviates slightly from a linear field dependence, which implies that some short-range FiM/FM interactions may occur in this temperature window since T_C is close to T_N.

The temperature-dependent ac magnetic susceptibility and specific heat were measured to further characterize the complex magnetism of CCCRO. As shown in Fig. 5(a), two peaks at T_N and T_C are apparent in the ac susceptibility. Moreover, the peak positions are independent of the applied measurement frequency [see the inset of Fig. 5(a)]. This demonstrates the long-range nature of both magnetic phase transitions. Figure 5(b) presents the specific heat measured at different fields. At 0 T, a sharp λ-type anomaly occurs at T_N. With

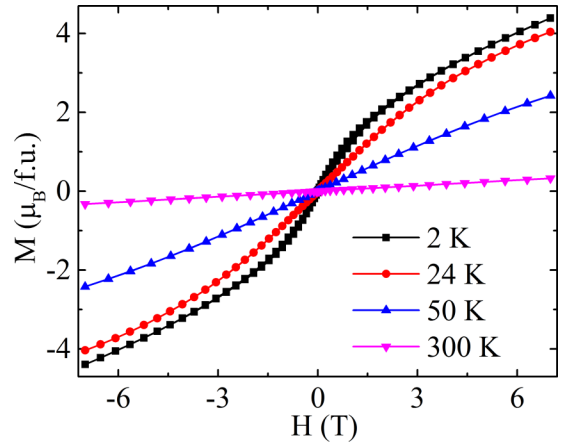

FIG. 4. Field-dependent magnetization measured at selected temperatures for CCCRO.

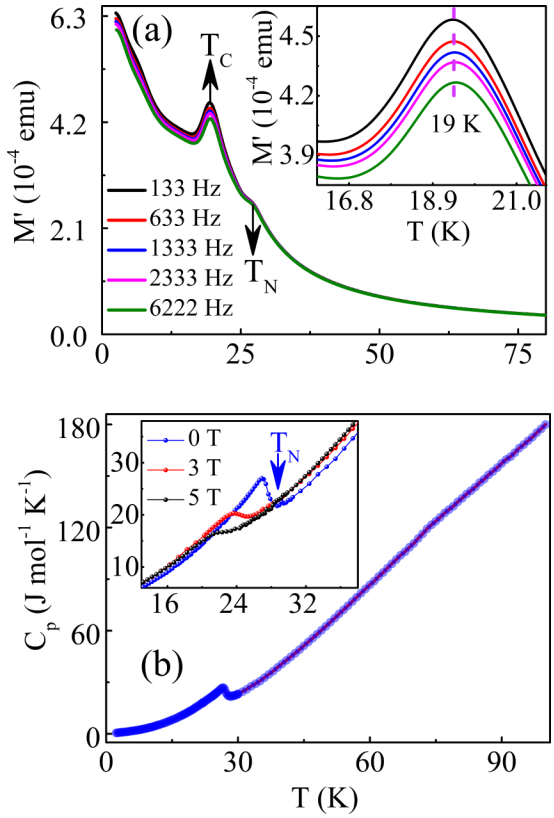

FIG. 5. (a) Temperature-dependent ac magnetization measured at different frequencies for CCCRO. The inset shows the enlarged view near T_C. (b) Temperature dependence of the specific heat at zero field. The inset shows the specific heat measured at different fields near T_N and T_C.

increasing field, the anomaly shifts toward lower temperatures (see inset). These features reflect the AFM ordering at T_N. Although the dc and ac susceptibility curves show a long-range FiM/FM phase transition at T_C, we do not find a clear anomaly in the specific heat near this critical temperature. This may be attributed to the similarity of T_C and T_N, so that most FiM/FM entropy change has already occurred between T_C and T_N.

In *A*-site ordered $ACu_3B_4O_{12}$ perovskites with nonmagnetic *B*-site cations, if the *B* site has empty *d* orbitals (e.g., as in Ti^{4+} or Zr^{4+}), then the *A*′-site Cu^{2+} sublattice can form long-range AFM ordering via the Cu-O-*B*-O-Cu super-superexchange interaction, as observed in $Ca/CdCu_3Ti_4O_{12}$ and $CaCu_3Zr_4O_{12}$ [9,16]. This means that the empty d^0 orbitals at the *B*-site can constitute an interaction pathway to trigger AFM ordering for the *A*′-site Cu^{2+} spins. Moreover, these compounds exhibit similar AFM phase transition temperatures at approximately 25–29 K. In the current CCCRO, the strong spin-orbital coupling of the 5*d* Re^{6+} ion separates the t_{2g} orbitals into $j = 3/2$ and $1/2$ bonds. Re^{6+} has a $5d^1$ electronic configuration with the electron partially occupying the $j = 3/2$ band and leaving the $j = 1/2$ band completely empty. This empty band may provide a super-superexchange pathway to form AFM ordering for the *A*′-site Cu^{2+} spins, as is the case for the d^0 orbitals in $Ca/CdCu_3Ti_4O_{12}$, so that the T_N of CCCRO is very similar to that reported for $Ca/CdCu_3Ti_4O_{12}$ and $CaCu_3Zr_4O_{12}$ [9,16]. Therefore, the AFM transition of CCCRO occurring at 28 K can most probably be ascribed to the spin ordering of the *A*′-site Cu^{2+} ions. On the other hand, the magnetic phase transition observed at 20 K in CCCRO should arise from the FM or FiM interaction between the high-spin Co^{2+} and Re^{6+} ions. Considering the spin moment only, the $Co^{2+}(\uparrow)Re^{6+}(\uparrow)$ FM coupling would produce a saturated moment as large as $8.0\,\mu_B$/f.u., much larger than the $4\,\mu_B$/f.u. observed from the experimental magnetization below 20 K at 6 T (see Fig. 4). In comparison, the $Co^{2+}(\uparrow)Re^{6+}(\downarrow)$ FiM coupling can give a saturated moment of $4.0\,\mu_B$/f.u. comparable to experiment. We thus conclude that a $Co^{2+}(\uparrow)Re^{6+}(\downarrow)$ FiM coupling is responsible for the spin phase transition occurring at 20 K in CCCRO.

Spin-spin coupling is directly observable in the XMCD measurements at the transition metal $L_{2,3}$ edges. Figure 6 shows the Cu-, Co-, and Re-$L_{2,3}$ edge XAS spectra measured using circularly polarized light, with the photon spin aligned parallel μ^+ (black line) or antiparallel μ^- (red line) to the magnetic field measured at 10 K. The magnetic field was 6 T for the Cu- and Co-$L_{2,3}$ edges and 1.3 T for the Re-$L_{2,3}$ edges. The XMCD spectra $\mu^+ - \mu^-$ are shown as blue lines. Firstly, a very large negative XMCD signal is visible at the Co-L_3 edge, and a weak positive XMCD signal at the Co-L_2 edge. The XMCD signal magnitude at the Co-$L_{2,3}$ edges is very similar to that observed in $CoFe_2O_4$ and $LaMn_{0.5}Co_{0.5}O_3$ [29,30]. In comparison, there is a relatively large negative XMCD signal at the Re-L_2 edge and a very weak positive XMCD signal at the Re-L_3 edge, indicating an FiM spin-spin coupling between Co and Re ions. The very small XMCD signal for Re indicates that the $Co^{2+}(\uparrow)Re^{6+}(\downarrow)$ FiM interaction is rather weak, consistent with the lower spin ordering temperature $T_C \sim 20$ K. The XMCD signal at the Cu-$L_{2,3}$ edges of CCCRO is much weaker than that observed in $CaCu_3Fe_2Re_2O_{12}$, where T_C reaches as high as 560 K owing to the stronger

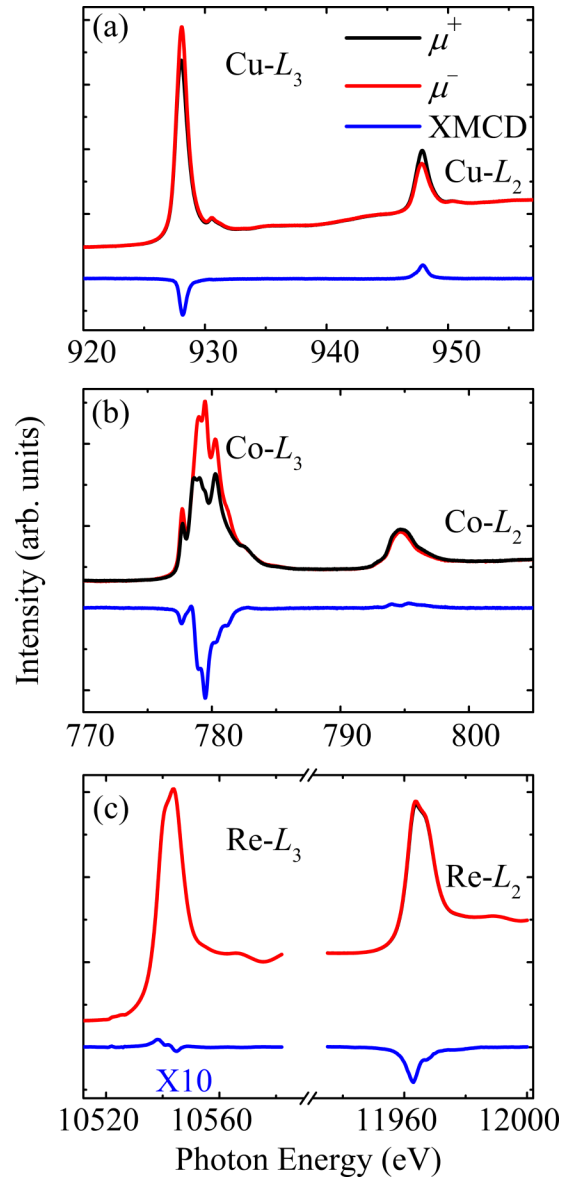

FIG. 6. XMCD for (a) Cu- and (b) Co-$L_{2,3}$ edges measured at 10 K and 6 T for CCCRO. The photon spin is aligned parallel (μ^+ black line) or antiparallel (μ^- red line) to the applied magnetic field. The difference spectra ($\mu^+ - \mu^-$) are shown as blue lines. (c) XMCD for Re-$L_{2,3}$ edges measured at 5 K and 5 T. The μ^- and μ^+ lines almost overlap because of the weak XMCD signal.

$Cu^{2+}(\uparrow)Fe^{3+}(\uparrow)Re^{5+}(\downarrow)$ FiM coupling [1]. This feature rules out FM coupling between Cu^{2+} ions, as a stronger XMCD signal would otherwise be expected. The XMCD results thus demonstrate that the Cu^{2+} sublattice causes AFM ordering at $T_N \sim 28$ K. The weak XMCD signal at the Cu-$L_{2,3}$ edges suggests there is a canted moment in a high magnetic field. In addition, it is interesting to compare the Co^{2+}/Re^{6+} magnetism of CCCRO with that observed in the $A_2Co^{2+}Re^{6+}O_6$ double-perovskite family with *A* = Ca, Sr, and Ba. Specifically, Ba_2CoReO_6 has a cubic $Fm\text{-}3m$ crystal structure with a 180° Co-O-Re bond angle, and shows noncollinear helical-type AFM ordering [31,32]. Sr_2CoReO_6 crystallizes in a tetragonal $I4/m$ crystal structure with an average

Co-O-Re bond angle of approximately 173 °. This compound shows *A*-type collinear AFM ordering [33]. A heavily distorted monoclinic $P2_1/n$ perovskite structure is found to occur in Ca_2CoReO_6, where the average Co-O-Re bond angle is approximately 150 ° [33]. However, this system displays FM-like behavior (the detailed spin alignment is unclear) [33]. This means that, with decreasing Co-O-Re bond angle, the magnetism of A_2CoReO_6 changes from noncollinear AFM to collinear AFM and then to FM-like behavior. In the current CCCRO, the Co-O-Re bond angle is further reduced to approximately 140 °. It also shows FM-like behavior due to the FiM $Co^{2+}(\uparrow)Re^{6+}(\downarrow)$ coupling, in accordance with the magnetic evolution of $A_2Co^{2+}Re^{6+}O_6$.

The orbital magnetic moment $M_{\rm orb}$ and the spin magnetic moment $M_{\rm spin}$ of Cu^{2+}, Co^{2+} and Re^{6+} can be estimated using the XMCD sum rules [34,35]

$$M_{\rm orb} = -\frac{4\int_{L_3+L_2}(\mu^+ - \mu^-)d\omega}{3\int_{L_3+L_2}(\mu^+ + \mu^-)d\omega}(10 - N_d), \tag{1}$$

$$M_{\rm spin} + 7\langle T_Z\rangle = -\frac{2\int_{L_3}(\mu^+ - \mu^-)d\omega - 4\int_{L_2}(\mu^+ - \mu^-)d\omega}{\int_{L_3+L_2}(\mu^+ + \mu^-)d\omega}(10 - N_d), \tag{2}$$

where $N_{\rm d}$ denotes the electron occupation number, and $\langle Tz\rangle$ the intra-atomic magnetic-dipole moment, which is negligible compared to $M_{\rm spin}$ in an octahedral symmetry coordination [35]. Using Eqs. (1) and (2), the orbital and spin moments are calculated as shown in Table II. Specifically, the total moments are 0.217 $\mu_{\rm B}$ per Cu^{2+}, 1.769 $\mu_{\rm B}$ per Co^{2+} (1.19 $\mu_{\rm B}$ from spin and 0.58 $\mu_{\rm B}$ from orbital), and −0.10 $\mu_{\rm B}$ per Re^{6+}. As a result, for each formula unit of CCCRO, the total magnetic moment calculated from the XMCD data is approximately 3.99 $\mu_{\rm B}$/f.u., similar to the magnetization measurement at 2 K and 6 T (4.02 $\mu_{\rm B}$/f.u.). The obtained moments of all three elements are obviously smaller than the expected values, indicating that CCCRO is not magnetically saturated even at 6 T as shown in Fig. 4. In such a case, it is preferred to extract the $M_{\rm orb}/M_{\rm spin}$ ratio for the Co^{2+} ion experimentally by using this formulation of the XMCD sum rule:

$$\frac{M_{\rm orb}}{M_{\rm spin} + 7\langle T_Z\rangle} = \frac{2}{3}\frac{\int_{L_3+L_2}(\mu^+ - \mu^-)d\omega}{\int_{L_3}(\mu^+ - \mu^-)d\omega - 2\int_{L_2}(\mu^+ - \mu^-)d\omega}. \tag{3}$$

This equation is more reliable than extracting the individual values for $M_{\rm orb}$ and $M_{\rm spin}$, since corrections are no longer necessary for an incomplete magnetization, for example, owing to the possible strong magnetocrystalline anisotropy in a polycrystalline material [29]. $M_{\rm orb}/M_{\rm spin}$ is approximately 0.48 as deduced from the Co-$L_{2,3}$ XMCD spectrum of CCCRO (see Table II). This indicates a large value of $M_{\rm orb}$, considering the generally large $M_{\rm spin}$ for the Co^{2+} ion. $M_{\rm spin}$ for a HS Co^{2+} was estimated to be 2.5 $\mu_{\rm B}$ in CoV_2O_6 and $LaMn_{0.5}Co_{0.5}O_3$ and 2.7 $\mu_{\rm B}$ in Ca_3CoRhO_6 [24,29,36]. The ratio $M_{\rm orb}/M_{\rm spin}$ in CCCRO is close to 0.47 for $LaMn_{0.5}Co_{0.5}O_3$, 0.49 for the γ phase of CoV_2O_6, but smaller than that for CoO (0.57) and the α phase of CoV_2O_6 (0.73) [29,36,37]. In any case, the estimated $M_{\rm orb}$ is approximately 1.2 $\mu_{\rm B}$ for CCCRO. It is also interesting to note that Cu^{2+} carries a substantial orbital moment with an $M_{\rm orb}/M_{\rm spin}$ of approximately 0.26 (see Table II). This is surprising since, usually, the Jahn-Teller Cu^{2+} ion with a $3d(x^2 - y^2)$ hole ground state does not carry any orbital moment. The fact that the Cu^{2+} in CCCRO has an orbital moment should then be attributed to a hybridization process with neighboring magnetic ions that have active spin orbit coupling interactions, so that the orbital moments of those neighboring ions can be transferred to Cu^{2+}. Indeed, with not only the Co but also the Re ions carrying a large orbital moment with $M_{\rm orb}/M_{\rm spin}$ approximately equal to 0.26 (see Table II), the presence of an orbital moment on the Cu can be taken as evidence for the superexchange mechanism between the Cu^{2+} ions taking place via the Re^{6+} and also the Co^{2+} ions.

To gain deeper insight into the AFM transition of the Cu^{2+} sublattice, we measured the XMCD around $T_{\rm N}$ and studied the intensity of the XMCD signal, which provides both the strength and sign of the magnetic coupling. As mentioned above, XMCD is element-selective, which therefore makes it a powerful method for studying the Cu and Co sublattices separately. Figures 7(a) and 7(b) show the magnitude of the XMCD signal and the value of the moment at the Cu-L_3 and Co-L_3 edges at different temperatures, respectively. One can see that the Co-L_3 XMCD signal monotonically increases upon cooling, indicating the FM coupling of Co spins, which are always parallel to the magnetic field. However, the Cu-L_3 XMCD signal behaves quite differently. Above 24 K, it also increases upon cooling, reaching a maximum at approximately 18 K, before then drastically decreasing upon further cooling down to 4 K. Thus, the Cu-L_3 XMCD spectrum provides solid evidence for an AFM transition happening for the Cu sublattice. We note that a magnetic field can always hamper AFM transitions, resulting in a decrease of the critical temperature, which can explain that the 6-T XMCD transition is near 18 K despite $T_{\rm N}$ being approximately 28 K for the

TABLE II. Orbital and spin moments of Cu^{2+}, Co^{2+}, and Re^{6+} in CCCRO, based on Eqs. (1) and (2), considering $N_{\rm d} = 9, 7, 1$ for Cu^{2+}, Co^{2+} and Re^{6+} ions, respectively. The XMCD signal for Re^{6+} was measured at 1.3 T, but at 6 T for Cu^{2+} and Co^{2+} ions.

Ion	$M_{\rm orb}(\mu_{\rm B}/{\rm atom})$	$M_{\rm spin}(\mu_{\rm B}/{\rm atom})$
Cu^{2+}	0.048	0.169
Co^{2+}	0.579	1.190
Re^{6+}	0.036	−0.138

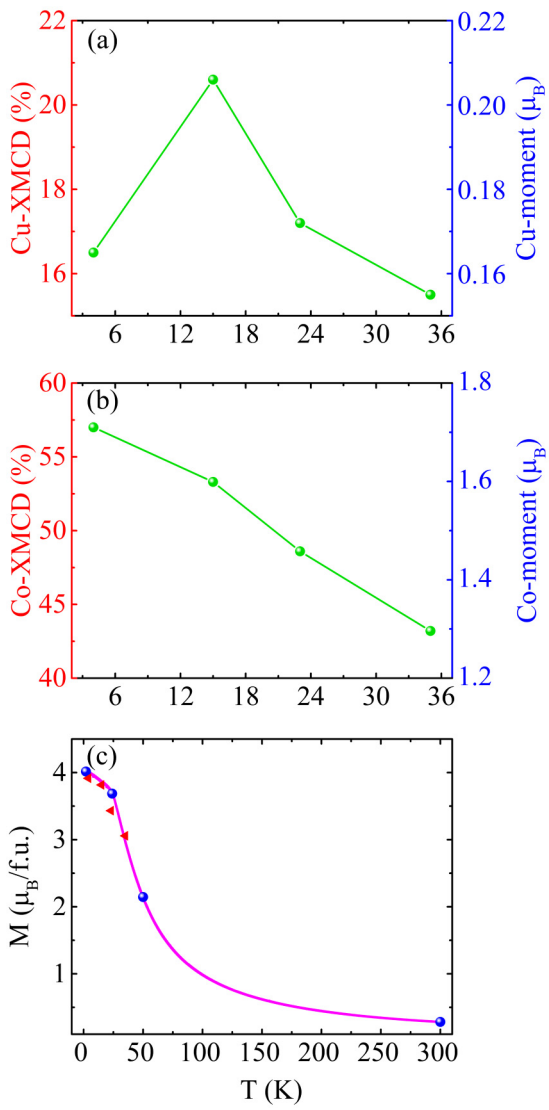

FIG. 7. XMCD magnitude at the (a) Cu- and (b) Co-$L_{2,3}$ edges measured at 6 T and different temperatures near T_N for CCCRO. (c) Magnetic moments measured at 6 T by different methods. The magenta line was obtained from the susceptibility, the blue dots from the magnetization, and the red triangles from XMCD measurements of Cu- and Co-$L_{2,3}$.

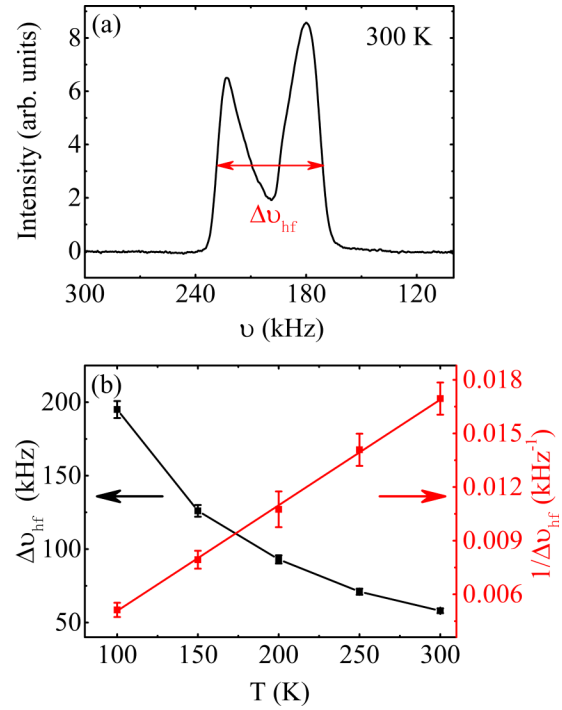

FIG. 8. (a) ^{63}Cu NMR spectrum of CCCRO measured at a magnetic field of 9.39 T and 300 K. The FWHM of central line ($\Delta\nu_{hf}$) is shown. (b) Temperature dependence of $\Delta\nu_{hf}$ and its inverse for ^{63}Cu NMR spectra.

susceptibility at 0.01 T [38]. Besides, in a unit cell, the total moments of Cu^{2+} and Co^{2+} calculated from the XMCD signal display the same trend and are comparable with the magnetization measurements, as shown in Fig. 7(c).

The ^{63}Cu NMR spectra of CCCRO were measured at variable temperatures and a magnetic field of 9.39 T. Figure 8(a) shows the spectrum collected at 300 K. The central line (transition $m_I = -1/2 \leftrightarrow 1/2$) splits into two sharp peaks due to second-order quadrupole interactions. The sharp feature indicates that Cu atoms are distributed with a high degree of order at *A* site, well consistent with the XRD refinement result. Figure 8(b) presents the temperature dependence of the full width at half maximum (FWHM) of central lines. With decreasing temperature, the value of FWHM ($\Delta\nu_{hf}$) increases monotonically. If one plots the inverse $\Delta\nu_{hf}$ as a function of temperature, it changes near linearly with temperature, similar with the temperature dependence of inverse susceptibility. This is in good agreement with the paramagnetic behavior of CCCRO at higher temperatures. However, as the temperature decreases below 50 K, the central line width becomes too broad to be measured completely. Such a broadening effect might be attributed to the development of some short-range spin correlations or inhomogeneous spin interactions at the high magnetic field we applied (9.39 T).

CCCRO exhibits a strong electrical insulating behavior so that the resistivity cannot be measured using a PPMS below 300 K. We therefore resorted to optical measurements to characterize the electrical properties. Figure 9 shows the UV-vis diffuse reflection spectrum measured at RT with decreasing wavelength. The spectrum shows a two-step-like sharp increase at the onsets about 260 and 220 nm, implying CCCRO to be an indirect semiconductor [39]. Based on the equation $(\alpha * E)^{1/2} = \mathrm{K}(E - E_g)$, where E and α denote the discrete photon energy and the absorption coefficient, respectively, the narrowest energy band gap is fitted to be $E_g = 3.75$ eV [39]. In the current *A*- and *B*-site ordered perovskite CCCRO, electrical transport is dominated by the corner-sharing CoO_6 and ReO_6 octahedra. The strong insulating feature with the large energy gap agrees well with the orderly distributed Co^{2+} and Re^{6+} without visible antisite occupancy. It is interesting to note that if Ca is replaced by La and some electrons are introduced into the Re site, half metallic behavior instead of strong insulating property occurs as recently reported in $LaCu_3Co_2Re_2O_{12}$ [40].

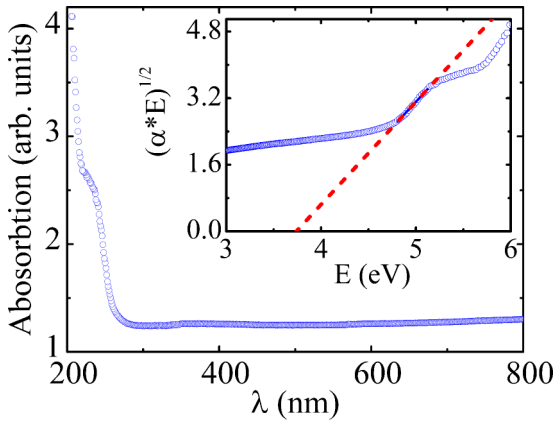

FIG. 9. UV-vis diffuse reflection spectrum for CCCRO collected at room temperature. The inset shows the Tauc plot of $(a * E)^{1/2}$ vs E.

IV. CONCLUSIONS

In summary, an oxide, $CaCu_3Co_2Re_2O_{12}$, was prepared by high-pressure and high-temperature at 7 GPa and 1323 K. XRD showed that the compound crystallizes as an A-site and B-site ordered cubic quadruple perovskite with Pn-3 symmetry. XAS measurements and a BVS calculation reveal the charge combination to be $CaCu^{2+}{}_3Co^{2+}{}_2Re^{6+}{}_2O_{12}$. This means that three different magnetic ions occupy three different atomic positions. The A'-site Cu^{2+} ions lead to a long-range AFM phase transition at approximately 28 K. In addition, FiM ordering is found to occur near 20 K as a result of the $Co^{2+}(\uparrow)Re^{6+}(\downarrow)$ coupling, as confirmed by XMCD results. Moreover, a large orbital moment is observed for Co^{2+}. As expected from the orderly distributed Co^{2+} and Re^{6+}, CCCRO shows strong electrical insulating behavior with a large energy band gap around 3.75 eV. This work reports a $ACu_3B_2B'_2O_{12}$ perovskite in which the A'-site Cu^{2+} ions contribute to long-range AFM ordering rather than a FM or FiM one as reported for other isostructural compounds.

ACKNOWLEDGMENTS

This work was supported by the National Key R&D Program of China (Grants No. 2018YFA0305700 and No. 2018YFE0103200), the National Natural Science Foundation of China (Grants No. 11934017, No. 51772324, No. 11921004, and No. 11574378), the Beijing Natural Science Foundation (Grant No. Z200007), and the Chinese Academy of Sciences (Grants No. XDB33000000, No. QYZDB–SSW–SLH013, and No. GJHZ1773). A portion of this work was performed on the Steady High Magnetic Field Facilities, High Magnetic Field Laboratory, CAS). The research in Dresden was partially supported by the DFG through SFB 1143 (Project-Id 247310070). We acknowledge the support from the Max Planck-POSTECH-Hsinchu Center for Complex Phase Materials. We acknowledge DESY (Hamburg, Germany), a member of the Helmholtz Association HGF, for the provision of experimental facilities. Parts of this research were carried out at beamline P09 at PETRA III at DESY using a 6T/2T/2T superconducting vector magnet funded in part under Grant No. 05K2013 by the Bundesministerium für Bildung und Forschung.

[1] W. T. Chen, M. Mizumaki, H. Seki, M. S. Senn, T. Saito, D. Kan, J. P. Attfield, and Y. Shimakawa, Nat. Commun. **5**, 3909 (2014).
[2] H. Deng, M. Liu, J. Dai, Z. Hu, C. Kuo, Y. Yin, J. Yang, X. Wang, Q. Zhao, Y. Xu, Z. Fu, J. Cai, H. Guo, K. Jin, T. Pi, Y. Soo, G. Zhou, J. Cheng, K. Chen, P. Ohresser, Y. F. Yang, C. Jin, L. H. Tjeng, and Y. Long, Phys. Rev. B **94**, 024414 (2016).
[3] X. Wang, M. Liu, X. Shen, Z. Liu, Z. Hu, K. Chen, P. Ohresser, L. Nataf, F. Baudelet, H. J. Lin, C. T. Chen, Y. L. Soo, Y. F. Yang, C. Jin, and Y. Long, Inorg. Chem. **58**, 320 (2019).
[4] Y. Shimakawa, Inorg. Chem. **47**, 19, 8562 (2008).
[5] I. Yamada, K. Takata, N. Hayashi, S. Shinohara, M. Azuma, S. Mori, S. Muranaka, Y. Shimakawa, and M. Takano, Angew. Chem. Int. Ed. **47**, 7032 (2008).
[6] Y. W. Long, N. Hayashi, T. Saito, M. Azuma, S. Muranaka, and Y. Shimakawa, Nature (London) **458**, 60 (2009).
[7] Z. Zeng, M. Greenblatt, M. A. Subramanian, and M. Croft, Phys. Rev. Lett. **82**, 3164 (1999).
[8] C. C. Homes, T. Vogt, S. M. Shapiro, S. Wakimoto, and A. P. Ramirez, Science **293**, 673 (2001).
[9] M. A. Pires, C. Israel, W. Iwamoto, R. R. Urbano, O. Agüero, I. Torriani, C. Rettori, P. G. Pagliuso, L. Walmsley, Z. Le, J. L. Cohn, and S. B. Oseroff, Phys. Rev. B **73**, 224404 (2006).
[10] X. Wang, Y. Chai, L. Zhou, H. Cao, C. D. Cruz, J. Yang, J. Dai, Y. Yin, Z. Yuan, S. Zhang, R. Yu, M. Azuma, Y. Shimakawa, H. Zhang, S. Dong, Y. Sun, C. Jin, and Y. Long, Phys. Rev. Lett. **115**, 087601 (2015).
[11] L. Zhou, J. Dai, Y. Chai, H. Zhang, S. Dong, H. Cao, S. Calder, Y. Yin, X. Wang, X. Shen, Z. Liu, T. Saito, Y. Shimakawa, H. Hojo, Y. Ikuhara, M. Azuma, Z. Hu, Y. Sun, C. Jin, and Y. Long, Adv. Mater. **29**, 1103435 (2017).
[12] Y. W. Long, T. Saito, M. Mizumaki, A. Agui, and Y. Shimakawa, J. Am. Chem. Soc. **131**, 16244 (2009).
[13] A. Prodi, E. Gilioli, A. Gauzzi, F. Licci, M. Marezio, F. Bolzoni, Q. Huang, A. Santoro, and J. W. Lynn, Nat. Mater. **3**, 48 (2004).
[14] H. Shiraki, T. Saito, T. Yamada, M. Tsujimoto, M. Azuma, H. Kurata, S. Isoda, M. Takano, and Y. Shimakawa, Phys. Rev. B **76**, 140403(R) (2007).
[15] R. Weht and W. E. Pickett, Phys. Rev. B **65**, 014415 (2001).
[16] M. Toyoda, K. Yamauchi, and T. Oguchi, Phys. Rev. B **87**, 224430 (2013).
[17] S. A. Larregola, J. Zhou, J. A. Alonso, V. Pomjakushin, and J. B. Goodenough, Inorg. Chem. **53**, 4281 (2014).
[18] M. S. Senn, W. T. Chen, T. Saito, S. García-Martín, J. P. Attfield, and Y. Shimakawa, Chem. Mater. **26**, 4832 (2014).
[19] S. H. Byeon, J. B. Parise, P. M. Woodward, and N. H. Hur, Chem. Mater. **17**, 3552 (2005).
[20] H. L. Feng, M. Arai, Y. Matsushita, Y. Tsujimoto, Y. Guo, C. I. Sathish, X. Wang, Y. H. Yuan, M. Tanaka, and K. Yamaura, J. Am. Chem. Soc. **136**, 3326 (2014).

[21] A. C. Larson and R. B. Von Dreele, *General Structure Analysis Aystem (GSAS)*, Report No. LAUR86-748 (Los Alamos National Laboratory, Los Alamos, NM, 1994).
[22] C. R. Wiebe, J. E. Greedan, P. P. Kyriakou, G. M. Luke, J. S. Gardner, A. Fukaya, I. M. Gat-Malureanu, P. L. Russo, A. T. Savici, and Y. J. Uemura, Phys. Rev. B **68**, 134410 (2003).
[23] L. H. Tjeng, C. T. Chen, and S. W. Cheong, Phys. Rev. B **45**, 8205(R) (1992).
[24] T. Burnus, Z. Hu, H. Wu, J. C. Cezar, S. Niitaka, H. Takagi, C. F. Chang, N. B. Brookes, H. J. Lin, L. Y. Jang, A. Tanaka, K. S. Liang, C. T. Chen, and L. H. Tjeng. Phys. Rev. B **77**, 205111 (2008).
[25] J. M. Chen, Y. Y. Chin, M. Valldor, Z. Hu, J. M. Lee, S. C. Haw, N. Hiraoka, H. Ishii, C. W. Pao, K. D. Tsuei, J. F. Lee, H. J. Lin, L. Y. Jang, A. Tanaka, C. T. Chen, and L. H. Tjeng, J. Am. Chem. Soc. **136**, 1514 (2014).
[26] Z. Hu, M. S. Golden, J. Fink, G. Kaindl, S. A. Warda, D. Reinen, P. Mahadevan, and D. D. Sarma, Phys. Rev. B **61**, 3739 (2000).
[27] Z. Hu, H. Wu, M. W. Haverkort, H. H. Hsieh, H. J. Lin, T. Lorenz, J. Baier, A. Reichl, I. Bonn, C. Felser, A. Tanaka, C. T. Chen, and L. H. Tjeng, Phys. Rev. Lett. **92**, 207402 (2004).
[28] J. H. Martin, G. Subias, J. Blasco, J. Garcia, and M. C. Sanchez, J. Phys.: Condens. Matter. **17**, 4963 (2005).
[29] T. Burnus, Z. Hu, H. H. Hsieh, V. L. J. Joly, P. A. Joy, M. W. Haverkort, H. Wu, A. Tanaka, H. J. Lin, C. T. Chen, and L. H. Tjeng, Phys. Rev. B **77**, 125124 (2008).
[30] Y. J. Chen, Y. H. Hsieh, S. C. Liao, Z. Hu, M. J. Huang, W. C. Kuo, Y. Y. Chin, T. M. Uen, J. Y. Juang, C. H. Lai, H. J. Lin, C. T. Chena, and Y. H. Chu, Nanoscale **5**, 4449 (2013).
[31] C. P. Khattak, D. E. Cox, and F. F. Y. Wang, in *Eighteenth Annual Conference on Magnetism and Magnetic Materials-1972*, edited by H. C. Wolfe, C. D. Graham, and J. J. Rhyne, AIP Conf. Proc. No. 10 (AIP, New York, 1973), p. 674.
[32] M. Musa Saad H. E. and N. Rammehb, Solid State Comm. **248**, 129 (2016).
[33] H. Kato, T. Okuda, Y. Okimoto, Y. Tomioka, K. Oikawa, T. Kamiyama, and Y. Tokura, Phys. Rev. B **69**, 184412 (2004).
[34] B. T. Thole, P. Carra, F. Sette, and G. van der Laan, Phys. Rev. Lett. **68**, 1943 (1992).
[35] P. Carra, B. T. Thole, M. Altarelli, and X. Wang, Phys. Rev. Lett. **70**, 694 (1993).
[36] N. Hollmann, S. Agrestini, Z. Hu, Z. He, M. Schmidt, C. Y. Kuo, M. Rotter, A. A. Nugroho, V. Sessi, A. Tanaka, N. B. Brookes, and L. H. Tjeng, Phys. Rev. B **89**, 201101(R) (2014).
[37] G. Ghiringhelli, L. H. Tjeng, A. Tanaka, O. Tjernberg, T. Mizokawa, J. L. de Boer, and N. B. Brookes, Phys. Rev B **66**, 075101 (2002).
[38] C. Stamm, J. U. Thiele, T. Kachel, I. Radu, P. Ramm, M. Kosuth, J. Minár, H. Ebert, H. A. Dürr, W. Eberhardt, and C. H. Back, Phys. Rev. B **77**, 184401 (2008).
[39] J. Zhang, F. J. Shi, J. Lin, D. F. Chen, J. M. Gao, Z. X. Huang, X. X. Ding, and C. C. Tang, Chem. Mater. **20**, 2937 (2008).
[40] Z. Liu, Q. Sun, X. Ye, X. Wang, L. Zhou, X. Shen, K. Chen, L. Nataf, F. Baudelet, S. Agrestini, C. Chen, H. Lin, H. B. Vasili, M. Valvidares, Z. Hu, Y. Yang, and Y. Long, Appl. Phys. Lett. **117**, 152402 (2020).